

MOLECULAR ENVIRONMENT OF THE SUPERNOVA REMNANT IC 443: DISCOVERY OF THE MOLECULAR SHELLS SURROUNDING THE REMNANT

YANG SU^{1,2}, MIN FANG^{1,2}, JI YANG^{1,2}, PING ZHOU³, AND YANG CHEN³

¹ Purple Mountain Observatory, Chinese Academy of Sciences, Nanjing 210008, China

² Key Laboratory of Radio Astronomy, Chinese Academy of Sciences, Nanjing 210008, China

³ Department of Astronomy, Nanjing University, Nanjing 210093, China

Draft version May 29, 2014

ABSTRACT

We have carried out ¹²CO, ¹³CO, and C¹⁸O observations toward the mixed morphology supernova remnant (SNR) IC 443. The observations cover a 1°5×1°5 area and allow us to investigate the overall molecular environment of the remnant. Some northern and northeastern partial shell structure of CO gas is around the remnant. One of the partial shells, about 5′ extending beyond the northeastern border of the remnant’s bright radio shell, seems to just confine the faint radio halo. On the other hand, some faint CO clumps can be discerned along the eastern boundary of the faint remnant’s radio halo. Connecting the eastern CO clumps, the northeastern partial shell structures, and the northern CO partial shell, we can see that a half molecular ring structure appears to surround the remnant. The LSR velocity of the half-ring structure is in the range of −5 km s^{−1} to −2 km s^{−1}, which is consistent with that of the −4 km s^{−1} molecular clouds. We suggest that the half-ring structure of the CO emission at $V_{\text{LSR}} \sim -4 \text{ km s}^{-1}$ is associated with the SNR. The structures are possibly swept up by the stellar winds of SNR IC 443’s massive progenitor. Based on the *Wide-field Infrared Survey Explorer* and the Two Micron All Sky Survey near-IR database, 62 young stellar object (YSO) candidates are selected within the radio halo of the remnant. These YSO candidates concentrated along the boundary of the remnant’s bright radio shell are likely to be triggered by the stellar winds from the massive progenitor of SNR IC 443.

Subject headings: ISM: individual (IC 443, G189.1+3.0) – ISM: molecules – supernova remnants

1. INTRODUCTION

Stars form from molecular clouds (MCs) and the stellar radiation and winds heavily sculpt their interstellar environment. When the massive star dies and explodes as a supernova, the remnant of it often evolves in such a complex environment. The distribution of the interstellar medium (ISM) and circumstellar medium in the vicinity of the supernova remnant (SNR) play an essential role for our understanding of the morphology and evolution of SNRs. Many SNR–MC interacting systems are investigated based on molecular observations, especially ¹²CO lines and their isotopes (Dickman et al. 1992; Seta et al. 1998).

SNR IC 443 (G189.1+3.0), an SNR–MC interacting system (e.g., DeNoyer 1979; Dickman et al. 1992; van Dishoeck et al. 1993), has been well studied in multi-wavelengths (see Shinn et al. 2011 for a recent review). Because of its large scale ($\sim 0^\circ 5$) and the lack of the confusion in the direction of the remnant, SNR IC 443 has become a good laboratory to study the astrophysical phenomena, e.g., the SNR–MC interaction, the relationship between the multiwavelength emission and the remnant’s evolution, the star formation activity near the remnant, and the origin of the cosmic rays in the vicinity of the SNR.

Braun & Strom (1986) suggested that SNR IC 443 has evolved inside the preexisting wind-blown bubble, which likely originated from the remnant’s massive progenitor star. This hypothesis was also supported by Troja et al. (2006, 2008) based on the analysis of *XMM-Newton* X-ray observations. According to 21 cm spectral-line and

continuum data, Lee et al. (2008) recently suggested that SNR IC 443 was into the western rarefied medium.

We performed new millimeter CO observations (covering about 2.25 deg²) toward the remnant to investigate the overall ambient MC distribution environing SNR IC 443. Based on the new CO observations, the half-ring structure in the velocity interval of −5 km s^{−1} to −2 km s^{−1} is probably associated with SNR IC 443. We also explore the possible physical connection between the half-ring structure and the stellar winds originating from the remnant’s massive progenitor star.

The paper is structured as follows. In Section 2, we show the CO observations and the data reduction. Sections 3 and 4 describe the main results and the physical discussion, respectively. A brief summary is given in Section 5.

2. OBSERVATIONS AND DATA REDUCTION

2.1. CO Data

The observations toward SNR IC 443 were made simultaneously in the ¹²CO ($J=1-0$) line (at 115.271 GHz), the ¹³CO ($J=1-0$) line (110.201 GHz), and the C¹⁸O ($J=1-0$) line (109.782 GHz) during 2011 November using the 13.7 m millimeter-wavelength telescope of the Purple Mountain Observatory at Delingha. It is a part of the Multi-Line Galactic Plane Survey in CO and its Isotopic Transitions, also called the Milky Way Imaging Scroll Painting, for the large-scale survey of dense molecular gas along the northern Galactic Plane. We used a new 3×3 pixel Superconducting Spectroscopic Array Receiver as the front end, which was made with

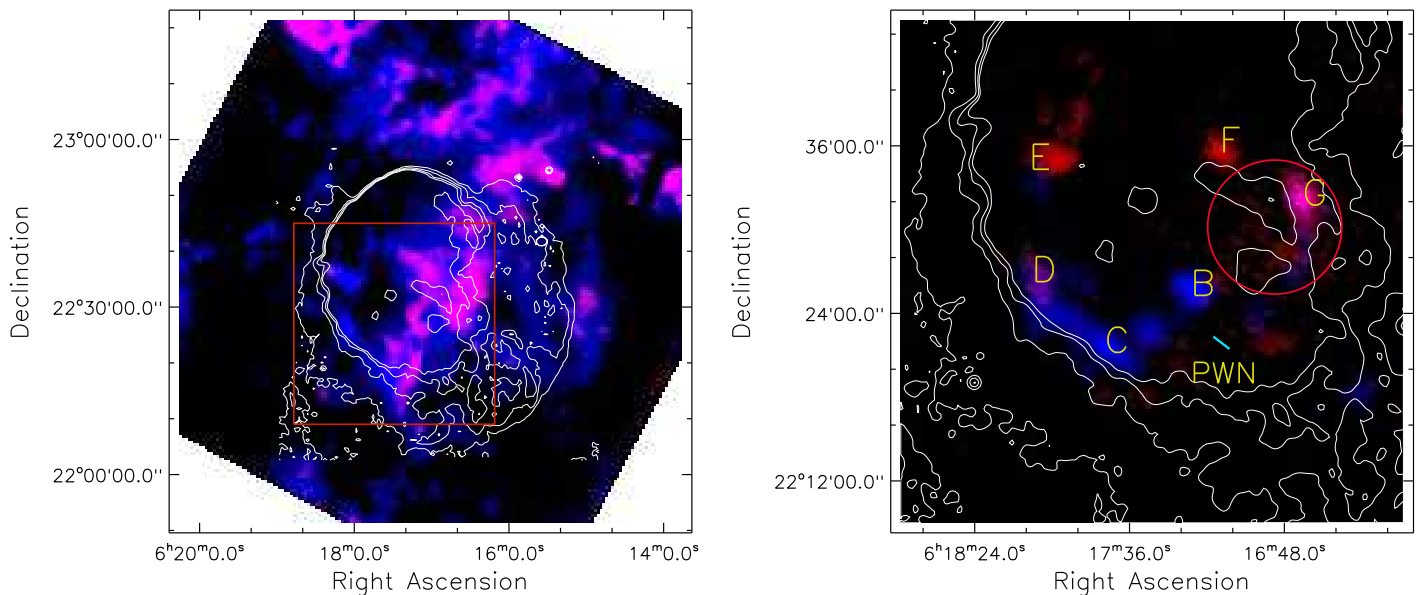


FIG. 1.— Left: ^{12}CO ($J=1-0$; blue) and ^{13}CO ($J=1-0$; red) intensity maps in the -10 km s^{-1} to 10 km s^{-1} interval with a square root scale toward SNR IC 443, overlaid with the 1.4 GHz radio continuum emission contours. The red box shows the area where the broadened molecular lines are detected (see right panel). Right: broadened ^{12}CO ($J=1-0$) integrated temperature map of SNR IC 443, overlaid with the 1.4 GHz radio continuum emission contours. The blue channel is in the -50 km s^{-1} to -9 km s^{-1} interval and the red is in the 0 km s^{-1} to 4 km s^{-1} interval. The letters B–G denote the location of the shocked clumps identified by Dickman et al. (1992). The red circle represents the location of the γ -ray source detected by VERITAS (Acciari et al. 2009), and the cyan line represents the location of the PWN detected by *Chandra* (Olbert et al. 2001).

Superconductor-Insulator-Superconductor (SIS) mixers using the sideband separating scheme (Shan et al. 2012; Zuo et al. 2011). An instantaneous bandwidth of 1 GHz was arranged for the backends. Each spectrometer provides 16,384 channels, resulting in a spectral resolution of 61 kHz, equivalent to a velocity resolution of about 0.16 km s^{-1} for ^{12}CO and 0.17 km s^{-1} for ^{13}CO and C^{18}O . The half-power beamwidth of the telescope is about $54''$ and the pointing accuracy of the telescope is greater than $4''$ in the observing epoch. We used the on-the-fly observing technique to map the $1.5^\circ \times 1.5^\circ$ area centered at $(l=189.0, b=3.0)$ with a scan speed of $50''\text{ s}^{-1}$ and a step of $15''$ along the Galactic longitude and latitude. The typical system temperature was around 200–330 K (120–170 K) for ^{12}CO (^{13}CO and C^{18}O) for each beam. The mean rms noise level of the brightness temperature (T_R) was less than 0.3 K for ^{12}CO and 0.2 K for ^{13}CO and C^{18}O . All of the CO data used in this study are expressed in brightness temperature, which are divided by the main beam efficiency $\eta_{\text{mb}} = 0.46$ ($T_R = T_A/(f_b \times \eta_{\text{mb}})$), assuming a beam filling factor of $f_b \sim 1$).

We have performed the largest ^{12}CO , ^{13}CO , and C^{18}O maps to date for such a moderately fine resolution, with fully sampled grids and low noise levels, which are essential to understand the large-scale environment of the remnant. All of the CO data were reduced using the GILDAS/CLASS package developed by IRAM.¹ Finally, the baseline-corrected spectra were converted to three-dimensional cube data with a grid spacing of $30''$ and a velocity channel separation of 0.2 km s^{-1} for subsequent analysis.

2.2. Infrared and Radio Data

The infrared (IR) photometric data used in this work were from the Two Micron All Sky Survey (2MASS; Skrutskie et al. 2006) and the survey of the *Wide-field Infrared Survey Explorer* (*WISE*, Wright et al. 2010). The 2MASS survey provides the near-IR photometry in the JHK_S bands with 10σ limiting magnitudes of ~ 15.8 , 15.1 , and 14.3 mag, respectively. The *WISE* survey covered the IC 443 region at the wavelengths of 3.4 , 4.6 , 12 , and $22\text{ }\mu\text{m}$ with spatial resolutions of $6''.1$, $6''.4$, $6''.5$, and $12''.0$, respectively. The 10σ limiting magnitudes are estimated to be ~ 15.7 , 14.7 , 10.4 , and 7.1 mag in the *WISE* $[3.4]$, $[4.6]$, $[12]$, and $[22]$ bands, respectively. In this work, we use two methods to select the sources. First, we select the sources with a signal-to-noise ratio (S/N) > 10 in the first three *WISE* bands given the spatial resolution of the $22\text{ }\mu\text{m}$ and that strong variable nebulae in the field of IC 443 make the photometry of faint sources very uncertain. Second, for those sources with a *WISE* $[12]$ band with an $S/N < 10$, we add the 2MASS JHK_S bands to select the young stellar object (YSO) candidates. We further reject any source suffering contamination or with confusion flags (cc_flag) as “D”, “H”, “O”, or “P” artifacts and only selected the point sources with ext_flag=0 (Koenig et al. 2012) to reduce the contamination emission by those extended sources. The detailed method is described by Koenig et al. (2012, see Appendices A.1–A.4 in their paper). The results of the selected disk-bearing young stellar population in the field of view (FOV) of SNR IC 443 are presented in Section 3.2.

The 1.4 GHz radio continuum emission data were obtained (Lee et al. 2008). The *Spitzer* $24\text{ }\mu\text{m}$ mid-IR observations were also used for comparison.

¹ <http://www.iram.fr/IRAMFR/GILDAS>

TABLE 1
 ^{13}CO ($J=1-0$) SPECTRAL PARAMETERS OF THE SHOCKED CLUMPS

Shocked Clumps Label	(R.A., Decl.) (J2000)	Extraction Area (arcmin)	$V_{\text{LSR}}(\text{Peak})$ (km s^{-1})	$T(\text{Peak})$ (K)
B	(06 ^h 17 ^m 16 ^s .8, 22°25′17″)	1×1	-3.0	0.9
C	(06 ^h 17 ^m 43 ^s .4, 22°21′13″)	1×1.5		
D	(06 ^h 18 ^m 06 ^s .0, 22°26′16″)	2×2.5	-7.8	0.3
E	(06 ^h 18 ^m 06 ^s .9, 22°34′19″)	1×1.5	-4.2	0.3
F	(06 ^h 17 ^m 07 ^s .8, 22°35′31″)	1×1	-3.4	1.5
G	(06 ^h 16 ^m 42 ^s .1, 22°31′46″)	1×1	-4.4	1.4

NOTE. — No ^{13}CO emission was detected for shocked clump C.

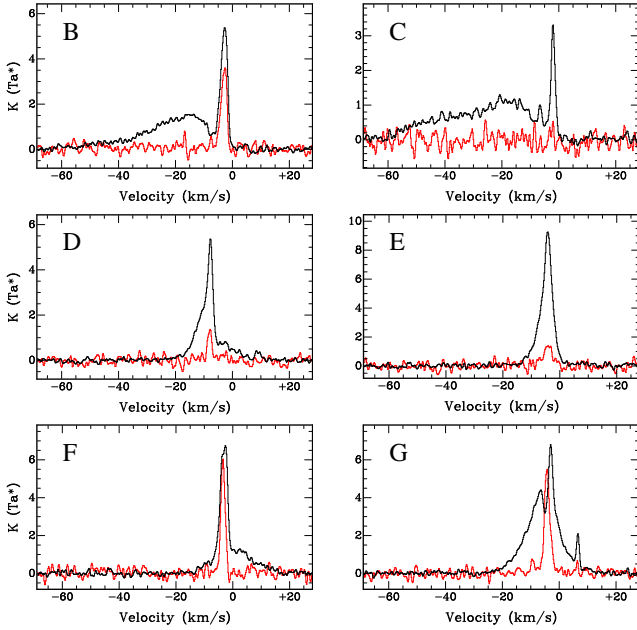


FIG. 2.— $^{12}\text{CO}(J=1-0)$; black) and $^{13}\text{CO}(J=1-0)$; red, multiplied by a factor of four) spectra of the shocked clumps B–G.

3. RESULTS

3.1. Molecular Emission

3.1.1. Global MC Distribution and the Shocked Molecular Clumps

^{12}CO ($J=1-0$), compared to ^{13}CO ($J=1-0$), usually show broad wings or asymmetric profiles that result from the shock perturbation of the molecular gas. Combining the emission of ^{12}CO ($J=1-0$) and ^{13}CO ($J=1-0$), we investigate the overall nature of the ambient molecular gas toward SNR IC 443.

Most of the ^{12}CO and ^{13}CO emission in the vicinity of SNR IC 443 arises from the velocity intervals of -50 km s^{-1} to 10 km s^{-1} and -10 km s^{-1} to 10 km s^{-1} , respectively. In Figure 1, we find that the molecular gas in the interval of -10 km s^{-1} to 10 km s^{-1} has a complicated distribution. On the contrary, the shocked gas in the interval of -50 km s^{-1} to -9 km s^{-1} and 0 km s^{-1} to 4 km s^{-1} , indicated by the broadened ^{12}CO , is mainly in the southeast and the center of the remnant, respectively. C^{18}O ($J=1-0$) emission is generally too weak to examine its spatial distribution, except that only some points with strong ^{13}CO emission were detected in the faint C^{18}O line, e.g., shocked clump G and small clouds

(SCs; named by Lee et al. 2012) 01, 03, 04, and 05.

We present the ^{12}CO and ^{13}CO spectra of shocked clumps B–G in Figure 2. The ^{13}CO lines show narrow Gaussian profiles (the red lines in Figure 2), while the ^{12}CO lines show broad wing profiles that represent the gas perturbed by the remnant’s shock (the black lines in Figure 2). In Table 1, we list the ^{13}CO parameters of shocked clumps B–G. We find that the LSR velocities of the ^{13}CO emission are around -4 km s^{-1} , except for clumps C and D (Table 1). For shocked clump C, we do not find the prominent ^{13}CO emission (Figure 2). On the other hand, the ^{13}CO emission of shocked clump D peaks at -7.8 km s^{-1} , which is consistent with the velocity of the adjacent OH 1720 MHz maser source (clump D, -6.85 km s^{-1} ; Hewitt et al. 2006). Shocked clumps C and D seem to form a long filament (about $13'$) along the southeastern bright radio border of SNR IC 443 (right panel of Figure 1). The emission of the shocked gas is more intense in the blueshifted side and mainly located along the southern boundary of the remnant. In contrast, the redshifted component is located in the center of the remnant. For shocked clump G, the position coincidence between the ^{13}CO line (-4.4 km s^{-1} ; Table 1 and Figure 2) and OH maser emission (-4.5 km s^{-1} ; Hewitt et al. 2006) toward it indicates that the gas emission with a similar LSR velocity arises from the same physical environment.

To investigate the detailed structures of the MCs toward SNR IC 443, we made an intensity weighted velocity (the first moment) map of ^{13}CO emission in the velocity range of -10 km s^{-1} to 10 km s^{-1} (Figure 3, left panel). We identify five ^{13}CO components in the FOV: -7 km s^{-1} ($V_{\text{LSR}}=-10 \text{ km s}^{-1}$ to -5 km s^{-1} , blue), -4 km s^{-1} ($V_{\text{LSR}}=-6 \text{ km s}^{-1}$ to -1 km s^{-1} , cyan), 3 km s^{-1} ($V_{\text{LSR}}=1.5 \text{ km s}^{-1}$ to 5 km s^{-1} , green), 5 km s^{-1} ($V_{\text{LSR}}=4 \text{ km s}^{-1}$ to 7 km s^{-1} , yellow), and 8 km s^{-1} ($V_{\text{LSR}}=7 \text{ km s}^{-1}$ to 9 km s^{-1} , orange). The typical spectra for different MC components are shown in Figure 4. The extraction region for these spectra are denoted in the left panel of Figure 3. The spatial distribution of the five velocity components can also be discerned in the first-moment maps of ^{13}CO (Figure 3). The -7 km s^{-1} ^{13}CO gas is mainly located to the north of the remnant. The 5 km s^{-1} gas can be divided into two parts: the eastern part is located in the southwest of the remnant and the western part along the western radio halo of the remnant. The 3 km s^{-1} MCs located to the northeast of the remnant and the 8 km s^{-1} MCs located to the east of the remnant seem not to be associated with the SNR.

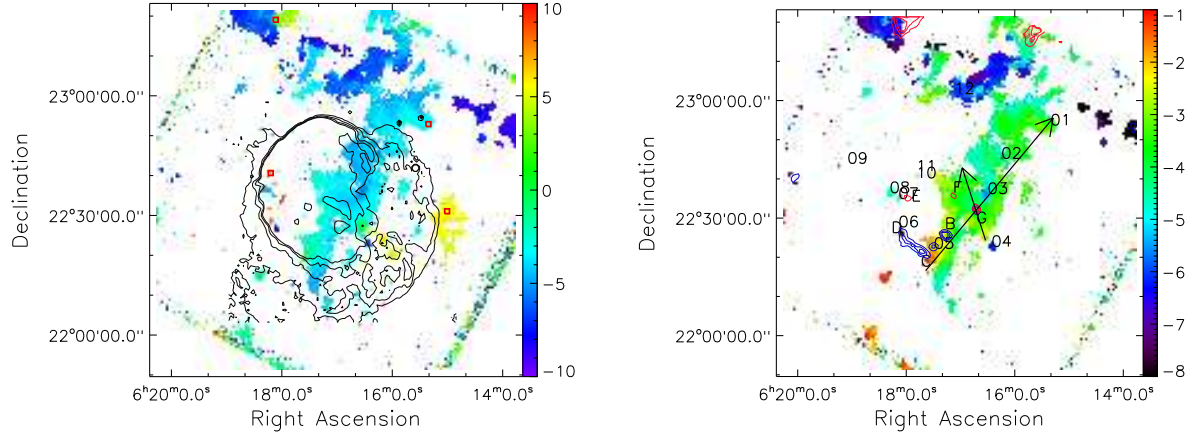


FIG. 3.— Left: the intensity weighted mean velocity (first moment) map of the ^{13}CO ($J=1-0$) emission in the interval of -10 km s^{-1} to 10 km s^{-1} , overlaid with the 1.4 GHz radio continuum emission contours. The four small red boxes indicate the regions from which the typical spectra for the five MC components are extracted (see Figure 4). Right: the intensity weighted mean velocity (first moment) map of the ^{13}CO emission in the interval of -8 km s^{-1} to -1 km s^{-1} . The numbers 01–12 denote the location of the SCs identified by Lee et al. (2012). The letters B–G denote the location of the shocked clumps and the blue and red contours show the blueshifted (-50 km s^{-1} to -9 km s^{-1}) and redshifted (0 km s^{-1} to 4 km s^{-1}) components, respectively (see Figure 1, right panel).

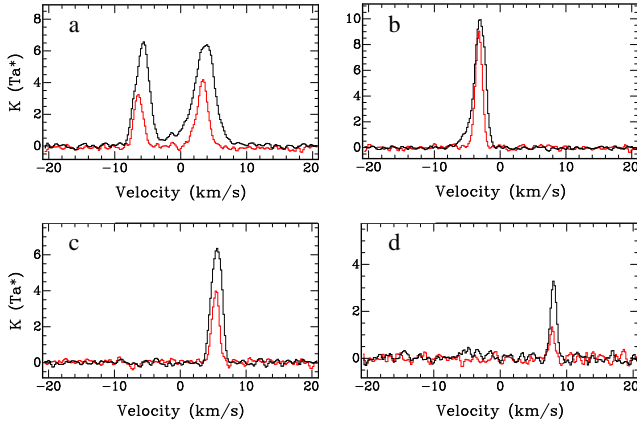


FIG. 4.— Typical ^{12}CO ($J=1-0$; black) and ^{13}CO ($J=1-0$; red, multiplied by a factor of two) spectra of the different MC components showing peaks at (a) -7 km s^{-1} and 3 km s^{-1} , (b) -3 km s^{-1} , (c) 5 km s^{-1} , and (d) 8 km s^{-1} , respectively. The spectra extraction regions are indicated by the small red box in Figure 3.

Notably, the prominent feature in the first moment map of the ^{13}CO emission is that the -4 km s^{-1} molecular gas extending along southeast–northwest divides the remnant into two parts: the multiwavelength bright part in northeast and the faint breakout in southwest. The -4 km s^{-1} MCs are mostly at the foreground of SNR IC 443 because of the evident absorption signature in the optical (Fesen 1984; Welsh & Sallmen 2003) and X-ray (Troja et al. 2006) bands. Also, some partial shell-like structures are located about $6'-10'$ to the north of the remnant and are projected concentrically with the northern radio border of SNR IC 443. To better investigate the velocity distribution of the -4 km s^{-1} molecular gas, we show the close-up intensity weighted velocity map of ^{13}CO emission in the -8 km s^{-1} to -1 km s^{-1} interval in the right panel of Figure 3, in which the location of the shocked clumps B–G and SCs 01–12 are denoted. The spectra of these SCs are shown in Figure 5.

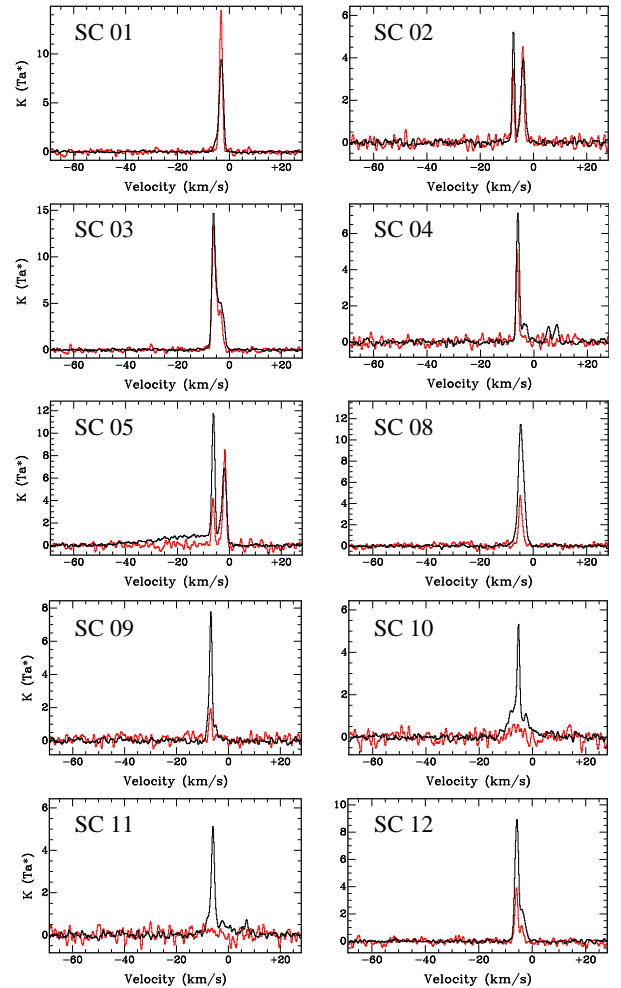


FIG. 5.— ^{12}CO ($J=1-0$; black) and ^{13}CO ($J=1-0$; red, multiplied by a factor of four) spectra of SCs 01–12. We do not show the spectra of SCs 06 and 07 because the spectra of the two SCs are similar to those of the shocked clumps D and E (see Figures 2 and 3).

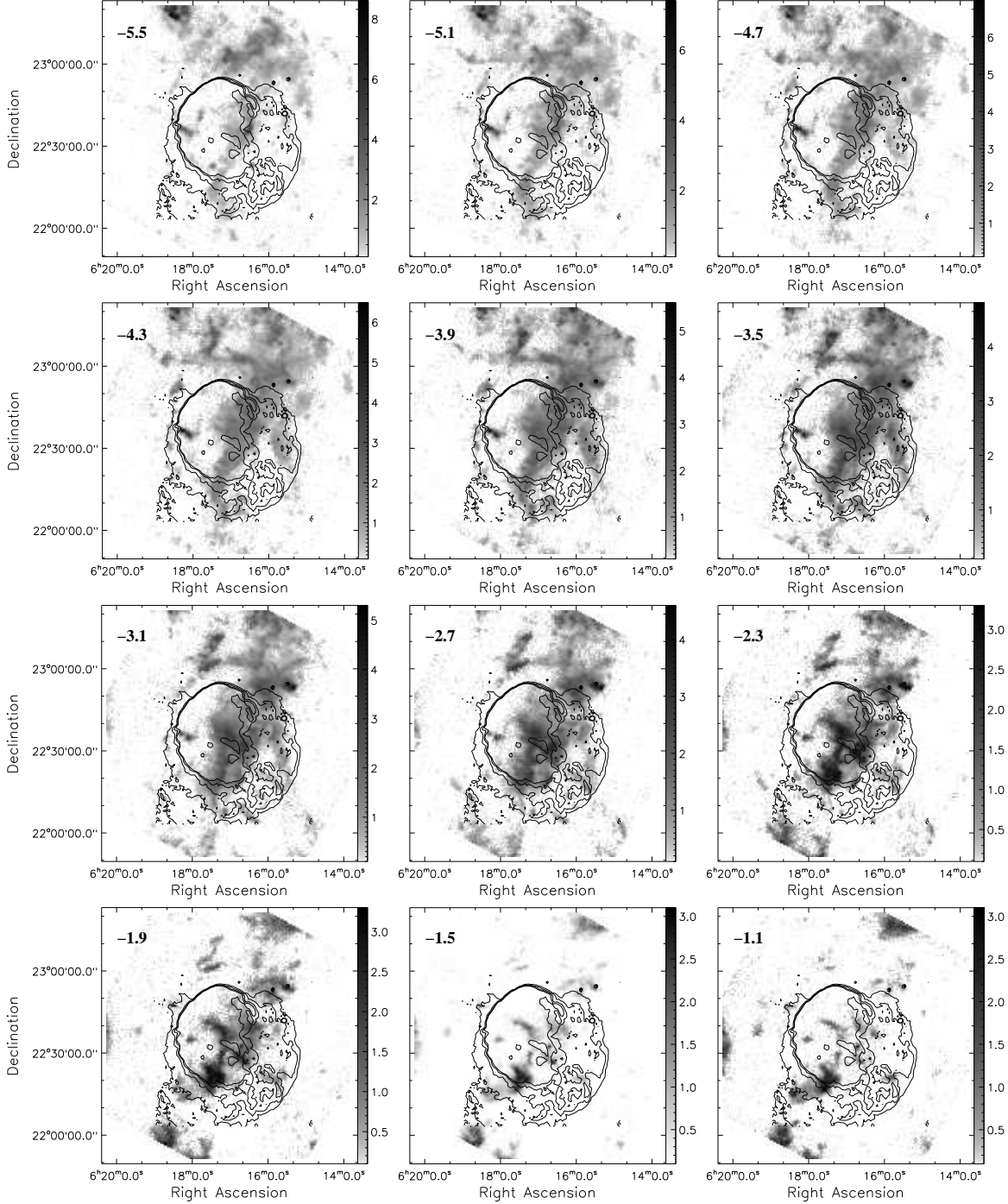


FIG. 6.— $^{12}\text{CO}(J=1-0)$ intensity channel maps in the velocity range between -5.5 km s^{-1} and -1.1 km s^{-1} , overlaid with the 1.4 GHz radio continuum emission contours. Note that the intensity scales are different from each other.

3.1.2. The Half Molecular Ring Structure Outside the SNR

We made the $^{12}\text{CO}(J=1-0)$ channel maps in a velocity interval of 0.4 km s^{-1} (Figure 6) in order to illustrate any tiny structures of the gas in the vicinity of the remnant for the -4 km s^{-1} MC component. By comparing the ^{12}CO images with the overlaid 1.4 GHz radio continuum contours, there are some partial shell structures outside the bright radio shell of the remnant's northeastern part ($\sim 5'$, approximately 2.2 pc at a typical distance of 1.5 kpc ; e.g., Fesen 1984; Braun & Strom 1986). The

northeastern partial shell structures can be discerned in -4.7 km s^{-1} to -3.1 km s^{-1} channel maps (Figure 6). We also find that a few ^{12}CO clumps are precisely located along the eastern boundary of the faint radio continuum halo (see also -4.7 km s^{-1} to -3.1 km s^{-1} channel maps in Figure 6). The faint halo structure appears outside the bright radio shell of SNR IC 443 and most likely originates from the interaction of the remnant with its environment (Lee et al. 2008). The similar radio halo can also be found in other SNRs, e.g., SNR 3C 391 (Reynolds

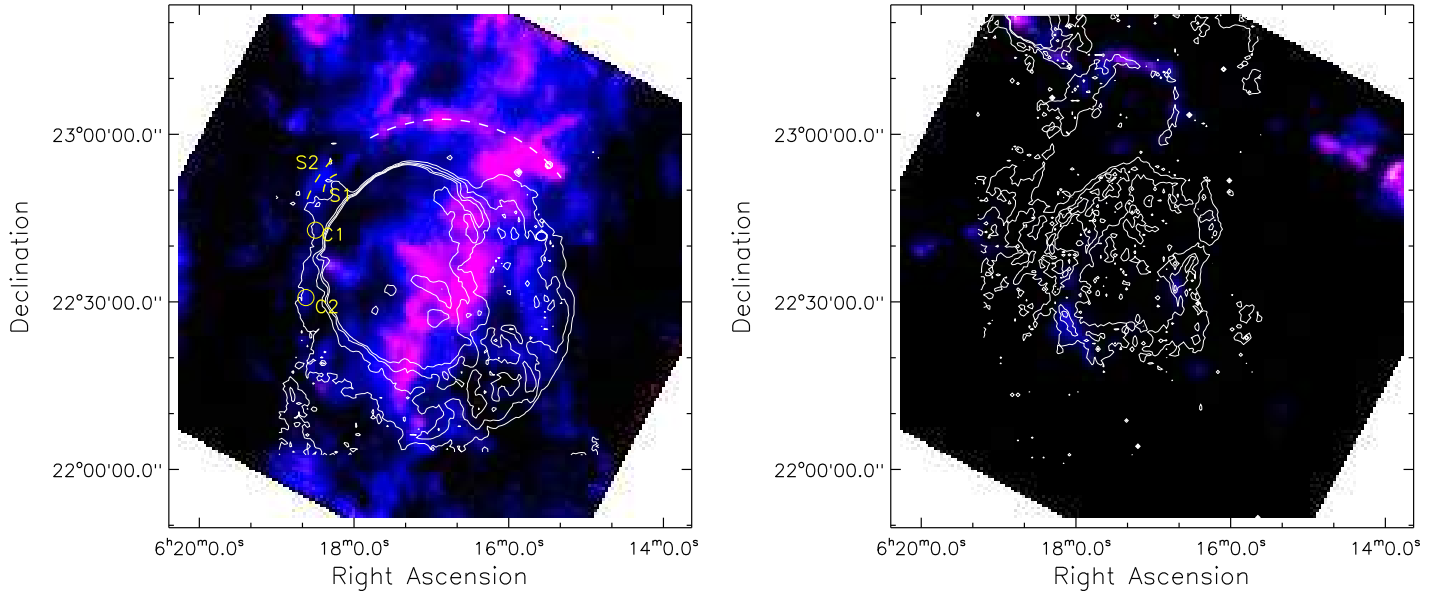


FIG. 7.— Left: the $^{12}\text{CO } J=1-0$ (blue) and $^{13}\text{CO } J=1-0$ (red) intensity maps in the -6 km s^{-1} to -1 km s^{-1} interval with the square root scale, overlaid with the 1.4 GHz radio continuum emission contours. The color scheme is adjusted to highlight the faint CO structures. The northern partial shell is denoted by the white dashed line. The northeastern partial shell structures (S1 and S2) and the eastern clumps (C1 and C2) are indicated in the image, the spectra of which are shown in Figure 8. The position-velocity map along the northern partial shell is shown in Figure 9. Right: ^{12}CO (blue) and ^{13}CO (red) intensity maps in the -9.2 km s^{-1} to -7.8 km s^{-1} interval with square root scale, overlaid with the *Spitzer* $24\mu\text{m}$ mid-IR emission contours.

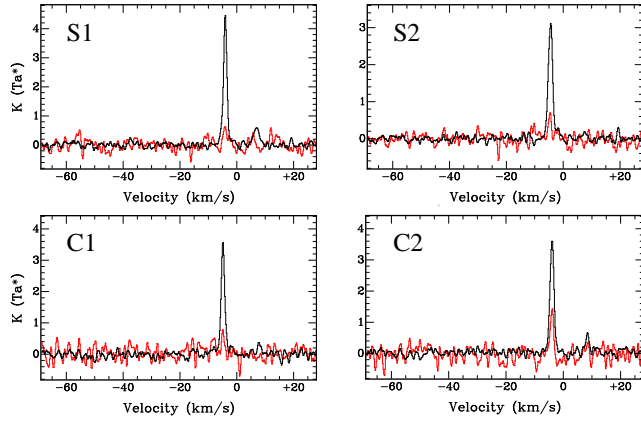


FIG. 8.— $^{12}\text{CO}(J=1-0)$; black and $^{13}\text{CO}(J=1-0)$; red, multiplied by a factor of four) spectra of S1, S2, C1, and C2 (see their locations in Figure 7).

& Moffett, 1993; Chen et al. 2004). The northern partial shell structure can be seen in -3.9 km s^{-1} to -1.9 km s^{-1} channel maps in Figure 6, similar to the structures found in the ^{13}CO first moment maps (the green arc in the right panel of Figure 3).

For subsequent analysis, we made the intensity maps of $^{12}\text{CO } (J=1-0)$ and $^{13}\text{CO } (J=1-0)$ in the -6 km s^{-1} to -1 km s^{-1} interval (Figure 7, left panel) to explore the distribution of the -4 km s^{-1} MCs around the SNR. In Figure 7, the northern partial shell structure, the northeastern partial shell structures (S1 and S2), and the eastern CO clumps (C1 and C2) are clearly seen and form a half ring to surround SNR IC 443. The half-

ring structure centered at $(06^{\text{h}}16^{\text{m}}57^{\text{s}}.1, 22^{\circ}37'06'')$ has a radius of $26'$. This position is close to the geometrical center of shell A, $(06^{\text{h}}17^{\text{m}}13^{\text{s}}, 22^{\circ}37'10'')$, suggested by Lee et al. (2008). The spectra of S1, S2, C1, and C2 are shown in Figure 8. Assuming that the line-of-sight depth of the partial shell structures is $\sim 1'$, we estimate the mean molecular density of the partial shell structures as $n(\text{H}_2) \sim 900 - 1300 \text{ cm}^{-3}$, which is consistent with the average molecular hydrogen densities of the SCs (Lee et al. 2012). In the above calculation, we adopt the mean CO-to- H_2 mass conversion factor of $1.8 \times 10^{20} \text{ cm}^{-2} \text{ K}^{-1} \text{ km}^{-1} \text{ s}$ (Dame et al. 2001) and the distance to the SNR of 1.5 kpc. For clump C1 and the partial shell structures S1 and S2, we did not use ^{13}CO information to estimate the column density because of their weak ^{13}CO emission (see Figure 8). For clump C2, assuming local thermodynamical equilibrium for the gas and an optically thick condition for the ^{12}CO line, we estimated the excitation temperature of the gas to be about 7 K and the optical depth of ^{13}CO to be about 0.11. Using the relation $N(\text{H}_2) = 7 \times 10^5 N(^{13}\text{CO})$ (Frerking et al. 1982), the column density of clump C2 we obtained is $\approx 5 \times 10^{20} \text{ cm}^{-2}$. Adopting the line-of-sight size of C2 $\sim 1'$, the mean molecular density is $n(\text{H}_2) \sim 400 \text{ cm}^{-3}$, which is less than the mean density from the X-factor method above. This is probably because of the low filling factor of weak ^{13}CO emission for those clumps. We did not calculate the mean density of the northern partial shell structure because the structure is mixed with the foreground/background CO emission.

In Table 2, we list the parameters of the ^{12}CO emission of the structures S1, S2, C1, and C2. The systemic LSR velocities of these structures are between -5 km s^{-1}

TABLE 2
 ^{12}CO ($J=1-0$) SPECTRAL PARAMETERS OF THE PARTIAL SHELL STRUCTURE

Shells/Clumps Label	(R.A., Decl.) (J2000)	Extraction Area (arcmin)	$V_{\text{LSR}}(\text{Peak})$ (km s^{-1})	$T(\text{Peak})$ (K)	W (K km s^{-1})
S1	(06 ^h 18 ^m 23 ^s .5, 22°51′39″)	3×1.5	-4.1	4.5	9.7
S2	(06 ^h 18 ^m 30 ^s .2, 22°51′55″)	7×1.5	-4.4	3.1	6.8
C1	(06 ^h 18 ^m 29 ^s .3, 22°42′45″)	1×1	-4.8	3.6	7.3
C2	(06 ^h 18 ^m 37 ^s .4, 22°30′43″)	1×1	-4.0	3.6	7.7

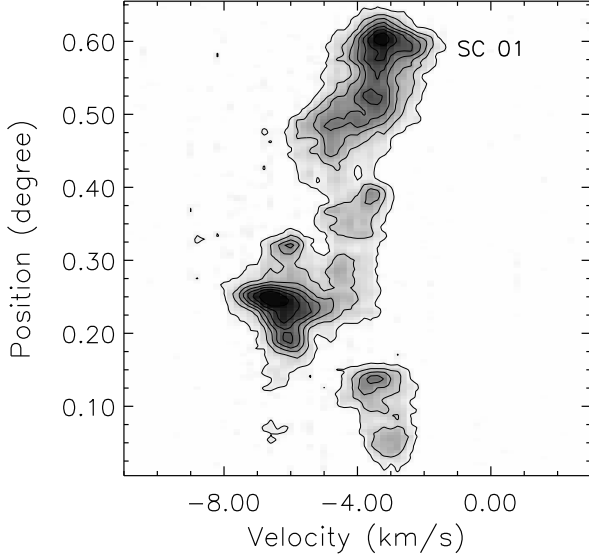


FIG. 9.— Position-velocity diagram of ^{13}CO emission along the northern partial shell structure. The position is measured from the east to the west along the white dashed line (see Figure 7) with a width of $2''.5$.

and -4 km s^{-1} . We also made the position-velocity (PV) diagram of ^{13}CO emission along the northern partial shell structure (Figure 9). We find that the velocity range of the shell spans from -5 km s^{-1} to -2 km s^{-1} , which is consistent with that of the first moment maps of ^{13}CO (Figure 3, right panel, the green arc to the north of the map). The additional prominent velocity component along the line of sight in this direction is -8 km s^{-1} to -5 km s^{-1} . This can also be seen in the first moment maps of the ^{13}CO emission (Figure 3, right panel, the blue part across the green arc to the north of the map). We emphasize here that the velocities of the partial shell structures are consistent with the velocity range of the -4 km s^{-1} MC component. They may belong to the -4 km s^{-1} MCs.

We discovered a faint CO bubble north of the remnant and centered at (06^h17^m17^s.3, 23°05′28″) with a diameter of $16'$, and in the velocity range of -9.2 km s^{-1} to -7.8 km s^{-1} (see the right panel of Figure 7), which is coincident with the bubble bright in the *Spitzer* $24\mu\text{m}$ mid-IR emission. The origin of the shell structure is unknown. In the $16'$ cavity, we have not found any massive stars in the SIMBAD Astronomical Database. However, a YSO candidate (J061718.39+230609.0, Class II) is found to be located near the center of the CO bubble.

3.2. YSO Distribution Near SNR IC 443

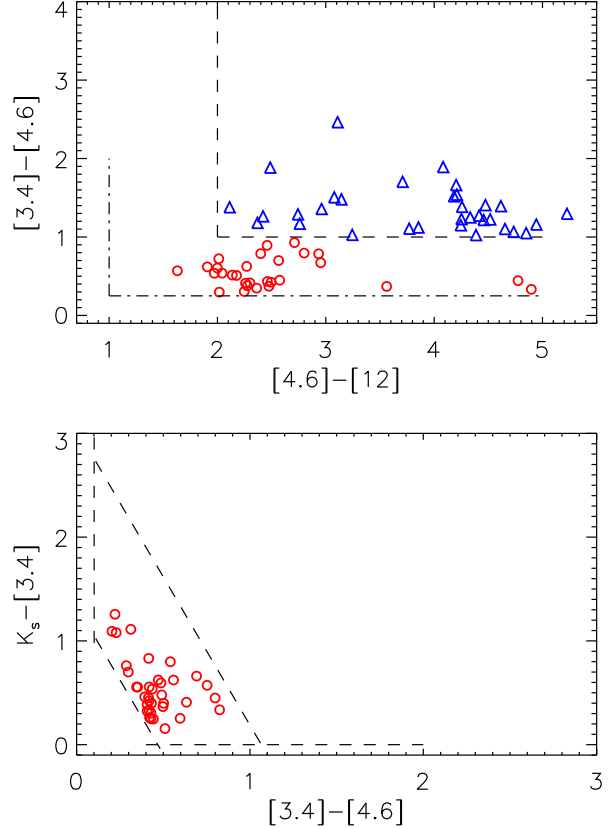


FIG. 10.— Upper: *WISE* band 1, 2, and 3 color-color diagram showing the distribution of YSO candidates (Class II: 29 red circles, see ID 1–29 in Table 3; Class I: 33 blue triangles, see ID 30–62 in Table 3) in the field of view of SNR IC 443. Lower: 2MASS K_s and *WISE* band 1 and 2 color-color diagram showing the distribution of YSO candidates (Class II: 36 red circles, see ID 63–98 in Table 3) in the field of view of SNR IC 443.

Using the IR data from the 2MASS and *WISE* surveys, we searched for the disk-bearing young star population in the field of IC 443. The dusty circumstellar disks can emit IR emission, which causes the IR colors of the disk-bearing young stars to be distinctly different from those of diskless objects. However, diskless young stars cannot be distinguished from unrelated field objects based on IR colors alone. Therefore, we only investigate the disk-bearing young stars in this study.

We selected candidate disk-bearing young stars using the criteria described in Koenig et al. (2012). The inventory of the young disk population is first based on the *WISE* $[3.4]-[4.6]$ versus $[4.6]-[12]$ color-color diagram (Figure 10, upper panel). We removed the contaminations from the extragalactic sources (star-forming galaxy and active galactic nuclei), the blobs of the shock emission, and the resolved polycyclic aromatic hydro-

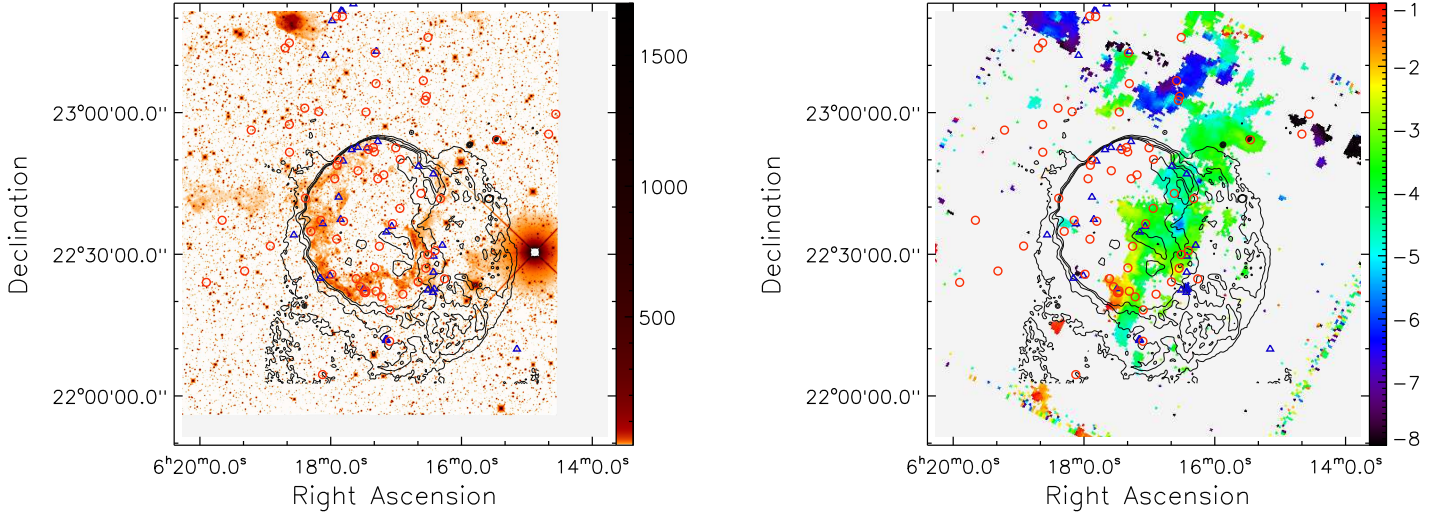


FIG. 11.— Left: the locations of the YSO candidates superimposed on the *WISE* 3.4 μm emission. The black contours are from the 1.4 GHz radio continuum emission. Right: the locations of the YSO candidates superimposed on the map of the first moment of the ^{13}CO emission in the interval of -8 to -1 km s^{-1} . The blue triangles are the YSO candidates of Class I, and the red circles are the YSO candidates of Class II.

carbon emission objects according to their locations in the $[3.4]-[4.6]$ versus $[4.6]-[12]$ color-color diagram and their *WISE* photometry (see the detailed description in Koenig et al. 2012). For the sources that were not detected in the *WISE* [12] band, their dereddened photometry in the *WISE* [3.4] and [4.6] bands, in combination of the dereddened 2MASS K_s photometry, was used to construct the $K_s-[3.4]$ versus $[3.4]-[4.6]$ color-color diagram (Figure 10, lower panel). The extinction used to deredden the photometry was estimated from its location in the $J-H$ versus $H-K_s$ color-color diagram as described in Fang et al. (2013).

In the $80' \times 80'$ area centered at $(l=189^\circ 0, b=3^\circ 0)$, we identified 98 (33 Class I and 65 Class II) potential YSOs from the *WISE*+2MASS color and the magnitude cuts imposed on the 15,077 sources with good S/N photometry. Figure 11 shows the locations of the YSO candidates on the *WISE* 3.4 μm map and the first moment of the ^{13}CO emission map, respectively. Sixty-two (24 Class I and 38 Class II) YSO candidates are located within the radio halo of SNR IC 443. We show the color-color diagrams of the YSO candidates in the FOV of SNR IC 443 (Figure 10) and list the information of the YSO candidates in Table 3. ID 1–29 are Class II YSO candidates (29 red circles in the upper panel of Figure 10) based on the *WISE* band 1, 2, and 3 color-color diagram. ID 30–62 are Class I YSO candidates (33 blue triangles in the upper panel of Figure 10) based on the *WISE* band 1, 2, and 3 color-color diagram. ID 63–98 are Class II YSO candidates (36 red circles in the lower panel of Figure 10) based on 2MASS K_s and the *WISE* band 1 and 2 color-color diagram. We also estimate the spectral slope, α , of the 98 sources from the IR spectral energy distributions (SEDs) to classify the evolutionary stages of these sources (Greene et al. 1994). We find that it is consistent with the result of the IR color-color method (Table 3).

The YSO candidates (Figure 11) are mostly distributed along the bright radio boundary, but are absent in the southwestern breakout portion of the remnant.

4. DISCUSSION

4.1. Association of SNR IC 443 with the $V_{\text{LSR}} \sim -4$ km s^{-1} MCs

The 1720 MHz OH maser is an important signpost of the interaction between SNRs and MCs (Lockett et al. 1999). For SNR IC 443, three OH masers were reported in Hewitt et al. (2006), and the locations of these three OH masers are close to the shocked clumps SC 05, D, and G, respectively. The three OH masers have velocities of -6.14 km s^{-1} , -6.85 km s^{-1} , and -4.55 km s^{-1} , respectively. These velocities represent the systemic velocities of the shocked gas that varies in a few kilometers per second. We found that there are two narrow ^{13}CO components with velocities centered at -6.4 km s^{-1} and -2.1 km s^{-1} in the shocked clump SC 05 and one narrow ^{13}CO component centered at -7.8 km s^{-1} in the shocked clump D. As two OH masers are adjacent to the two shocked clumps, the -6.4 km s^{-1} and -7.8 km s^{-1} components of the ^{13}CO emission are likely due to the preshock gas while the -2.1 km s^{-1} component might be from the foreground/background MC along the line of sight. The -4 km s^{-1} MCs seems to divide the remnant into the multiwavelength bright part in northeast and the faint breakout part in southwest. It is noteworthy that the shocked clump G is projected around the centroid of the -4 km s^{-1} MCs extending along the southeast-northwest. Figure 12 shows PV diagrams of ^{12}CO and ^{13}CO across the shock clump G along the southwest-northeast (the short arrow in the right panel of Figure 3). The LSR velocity coincidence between the ^{13}CO line and OH maser emission toward the shocked clump G (see Section 3.1.1) indicates that the -4 km s^{-1} molecular gas could be associated with SNR IC 443 (Figure 12).

TABLE 3 The Infrared Photometric Magnitudes of the YSO Candidates toward SNR IC 443

ID	Catalog Number	$J(1.25\mu\text{m})$ (mag)	$H(1.65\mu\text{m})$ (mag)	$K_S(2.17\mu\text{m})$ (mag)	$W1(3.4\mu\text{m})$ (mag)	$W2(4.6\mu\text{m})$ (mag)	$W3(12\mu\text{m})$ (mag)	$W4(22\mu\text{m})$ (mag)	A_v (mag)	α
1	J061635.03+230645.3	14.31±0.03	13.25±0.04	12.43±0.02	11.57±0.02	11.00±0.02	9.37±0.05	7.10±0.10	0.86	-1.22
2	J061837.94+231445.7	15.32±0.06	14.14±0.06	13.61±0.04	12.84±0.03	12.12±0.03	10.11±0.08	8.81±0.00	4.97	-1.06
3	J061841.76+231341.3	14.60±0.04	13.58±0.03	12.91±0.03	12.08±0.03	11.57±0.02	9.39±0.06	7.25±0.14	1.48	-0.97
4	J061630.72+231555.9	14.47±0.04	13.36±0.04	12.95±0.03	12.21±0.03	11.59±0.02	9.68±0.08	7.71±0.18	3.93	-1.17
5	J061754.79+232025.6	16.34±0.11	14.98±0.09	14.11±0.04	13.15±0.03	12.22±0.03	9.51±0.07	6.86±0.08	4.68	-0.43
6	J061741.61+232436.4	15.95±0.07	14.55±0.06	13.60±0.03	12.67±0.03	11.88±0.03	9.48±0.05	7.30±0.13	4.56	-0.71
7	J061719.17+231237.1	14.98±0.04	13.73±0.04	12.92±0.03	11.82±0.02	11.28±0.02	9.31±0.07	6.69±0.07	3.52	-1.01
8	J061718.39+230609.0	13.81±0.03	13.08±0.03	12.35±0.02	11.31±0.02	10.68±0.02	8.41±0.03	6.37±0.07	0.00	-0.72
9	J061632.20+230327.2	15.49±0.05	14.23±0.05	13.45±0.03	12.61±0.03	11.82±0.02	8.89±0.04	6.54±0.06	4.21	-0.43
10	J061705.93+221134.7	14.23±0.03	13.60±0.04	13.40±0.04	13.07±0.03	12.66±0.04	10.40±0.10	8.39±0.00	0.00	-1.17
11	J061837.93+225728.6	13.95±0.03	13.07±0.03	12.48±0.02	11.69±0.02	11.27±0.02	8.77±0.03	6.80±0.10	0.15	-0.82
12	J061440.06+225527.0	14.93±0.04	13.87±0.04	13.31±0.03	12.83±0.03	12.48±0.04	10.12±0.07	7.35±0.14	4.20	-1.19
13	J061656.51+223943.2	14.01±0.04	13.19±0.04	12.50±0.03	11.18±0.02	10.66±0.02	8.53±0.03	5.96±0.06	0.00	-0.74
14	J061716.73+224559.9	13.91±0.03	13.32±0.03	12.86±0.02	12.23±0.03	11.86±0.03	8.30±0.03	5.58±0.04	0.00	-0.30
15	J061700.34+225232.0	14.65±0.04	13.77±0.04	13.35±0.03	12.97±0.03	12.60±0.03	10.12±0.07	6.39±0.06	2.55	-1.11
16	J061653.86+222132.7	15.23±0.05	14.52±0.06	14.24±0.05	13.90±0.04	13.23±0.06	10.28±0.10	8.34±0.33	0.73	-0.62
17	J061630.86+222955.8	13.73±0.03	13.05±0.04	12.91±0.03	12.68±0.03	12.30±0.03	10.03±0.10	8.70±0.00	0.75	-1.24
18	J061748.23+223659.3	13.98±0.03	13.65±0.05	13.47±0.04	13.06±0.03	12.61±0.03	10.04±0.08	7.26±0.11	0.00	-0.92
19	J061619.31+224145.5	15.92±0.07	14.95±0.07	14.77±0.08	14.04±0.05	13.71±0.06	8.81±0.05	7.09±0.12	3.45	0.41
20	J061759.05+222546.6	12.97±0.03	12.74±0.03	12.60±0.03	12.37±0.03	12.07±0.04	10.05±0.09	7.78±0.21	0.00	-1.42
21	J061837.82+225136.7	14.30±0.04	13.86±0.05	9.08±0.05	7.19±0.14	...	1.17
22	J061823.79+230056.5	13.25±0.04	12.65±0.05	12.05±0.03	11.28±0.02	10.86±0.02	8.56±0.03	6.34±0.06	...	-0.94
23	J061727.79+222214.7	15.02±0.04	13.84±0.03	13.26±0.03	12.63±0.03	11.83±0.03	9.03±0.11	6.68±0.09	5.32	-0.63
24	J061855.42+223144.8	15.70±0.06	14.62±0.07	13.73±0.04	12.77±0.03	12.17±0.03	10.17±0.10	8.16±0.33	0.56	-0.94
25	J061912.92+225617.5	14.94±0.05	14.10±0.05	13.69±0.04	12.94±0.03	12.40±0.03	10.36±0.10	7.90±0.21	2.27	-1.09
26	J061719.72+222707.3	14.69±0.04	13.72±0.03	13.28±0.03	12.50±0.03	11.80±0.02	9.23±0.04	7.90±0.28	3.20	-0.70
27	J061632.71+222702.3	13.54±0.03	13.15±0.04	13.03±0.02	12.80±0.03	12.36±0.03	9.90±0.10	7.77±0.22	0.00	-1.07
28	J061713.00+222058.8	14.24±0.03	13.34±0.03	12.94±0.02	12.61±0.03	12.31±0.03	10.06±0.09	8.45±0.00	2.60	-1.31
29	J061734.95+224741.7	15.12±0.05	14.40±0.06	14.22±0.05	13.71±0.04	12.81±0.07	10.36±0.10	7.56±0.22	0.21	-0.68
30	J061805.00+231208.0	15.66±0.07	14.47±0.07	13.52±0.04	11.93±0.02	10.90±0.02	7.65±0.02	4.78±0.03	1.64	0.29
31	J061749.29+232130.7	14.79±0.04	14.27±0.05	13.94±0.04	12.83±0.03	11.73±0.02	7.96±0.02	5.78±0.04	0.00	0.47
32	J061758.83+231928.2	15.20±0.04	13.31±0.04	11.99±0.02	10.81±0.03	9.63±0.02	7.26±0.02	4.79±0.03	8.60	-0.49
33	J061739.23+232302.4	16.53	15.51	14.19±0.07	11.88±0.03	10.00±0.02	7.51±0.02	4.83±0.04	...	0.72
34	J061718.10+231300.1	13.71±0.03	12.24±0.03	9.09±0.04	6.10±0.05	...	0.46
35	J061750.41+232135.6	16.76±0.15	15.52±0.16	14.83±0.09	13.53±0.03	12.24±0.03	9.49±0.06	6.42±0.06	5.73	-0.08
36	J061742.01+232423.4	17.36	15.44	15.19±0.13	13.87±0.03	12.61±0.03	10.18±0.10	8.23±0.41	...	-0.12
37	J061709.15+221145.0	15.46±0.09	13.92±0.06	9.71±0.06	8.25±0.31	...	1.35
38	J061729.73+222242.5	13.72±0.04	11.26±0.03	8.15±0.03	5.17±0.04	...	1.00
39	J061625.78+224701.3	15.63±0.10	14.53±0.11	9.87±0.08	7.70±0.21	...	1.46
40	J061708.88+223443.3	15.40±0.06	14.13±0.07	9.72±0.06	8.65±0.00	...	1.36
41	J061509.13+220956.3	16.52±0.12	15.41±0.10	14.76±0.09	12.91±0.03	11.55±0.02	8.59±0.03	6.36±0.07	3.03	0.40
42	J061809.61+222455.5	15.34±0.08	14.09±0.08	9.75±0.09	8.35±0.00	...	1.28
43	J061626.00+222156.5	15.09±0.06	13.87±0.07	9.35±0.06	7.55±0.20	...	1.42
44	J061735.17+225237.3	14.79±0.07	13.76±0.09	9.38±0.11	7.70±0.41	...	1.20
45	J061624.95+222239.6	15.86±0.10	14.56±0.09	9.33±0.07	7.75±0.24	...	2.03
46	J061807.22+223628.7	14.59±0.11	13.07±0.07	8.88±0.05	7.82±0.30	...	1.32
47	J061709.33+221159.0	15.62±0.09	14.56±0.10	9.82±0.07	8.51±0.36	...	1.50
48	J061625.75+222612.2	15.60±0.10	14.19±0.09	9.72±0.09	8.01±0.28	...	1.49
49	J061625.62+222937.0	16.80±0.15	14.32±0.06	12.74±0.02	11.05±0.02	9.55±0.02	6.47±0.02	4.16±0.02	14.73	0.18
50	J061617.53+223155.7	16.87	15.36±0.11	13.64±0.04	12.33±0.02	10.95±0.02	8.84±0.03	5.97±0.05	...	-0.24
51	J061726.78+225232.8	15.09±0.09	13.95±0.09	9.70±0.08	7.41±0.22	...	1.16
52	J061748.60+224945.5	15.50±0.10	13.84±0.09	9.64±0.07	7.53±0.23	...	1.42
53	J061750.93+223723.3	15.26±0.08	13.88±0.07	9.62±0.06	7.49±0.16	...	1.30
54	J061740.69+225208.9	16.26	15.78	15.39±0.16	13.81±0.05	12.69±0.04	8.84±0.05	6.25±0.09	...	0.74
55	J061639.32+224839.1	15.48±0.07	14.08±0.06	9.47±0.04	6.74±0.08	...	1.59
56	J061800.63+222529.0	15.35±0.09	13.46±0.06	9.38±0.06	8.14±0.53	...	1.45
57	J061716.87+225352.2	15.73±0.09	14.57±0.10	9.63±0.06	6.49±0.08	...	1.72
58	J061630.87+222225.3	15.58±0.08	14.37±0.08	9.91±0.08	8.59±0.43	...	1.36
59	J061833.83+223406.1	13.74±0.03	12.57±0.03	9.81±0.07	7.51±0.17	...	-0.02
60	J061752.68+224206.8	17.14±0.22	15.93±0.17	15.76±0.21	14.74±0.09	13.52±0.09	9.27±0.04	8.33±0.00	5.78	0.64
61	J061708.62+221156.3	15.56±0.09	14.51±0.09	9.66±0.06	7.39±0.12	...	1.58
62	J061703.93+223554.7	14.97±0.08	13.27±0.06	9.56±0.07	8.32±0.30	...	1.05
63	J061433.46+225940.2	11.75±0.03	11.22±0.03	10.77±0.02	10.22±0.02	9.87±0.02	9.00±0.03	8.15±0.27	0.00	-1.91
64	J061803.57+232837.9	16.52±0.19	15.54±0.18	14.99±0.14	13.62±0.03	13.36±0.04	10.11±0.07	7.47±0.12	2.97	-0.30
65	J061749.30+232018.8	17.04±0.18	15.62±0.13	14.91±0.09	14.15±0.04	13.64±0.05	10.79±0.22	7.88±0.19	7.50	-0.77
66	J061742.48+232427.5	17.02±0.19	15.52±0.12	15.06±0.09	14.35±0.04	13.75±0.06	11.39±0.30	7.94±0.00	8.45	-1.05
67	J061615.59+222447.8	15.05±0.05	14.34±0.06	14.09±0.06	13.67±0.03	13.23±0.04	11.47±0.24	8.71±0.00	0.50	-1.41
68	J061729.18+222152.8	14.85±0.03	13.85±0.04	13.31±0.03	12.56±0.04	12.03±0.04	10.26	8.17±0.28	3.60	...
69	J061732.84+222308.1	13.59±0.03	13.07±0.03	12.80±0.03	12.54±0.06	12.11±0.10	9.66±0.27	7.87±0.24	0.00	-1.08
70	J061527.24+225413.5	15.62±0.06	14.63±0.06	14.02±0.05	13.40±0.03	13.03±0.03	9.81±0.07	7.29±0.11	1.53	-0.55
71	J061705.63+221812.7	14.98±0.04	14.41±0.06	14.09±0.05	13.69±0.03	13.19±0.04	11.48±0.29	8.17±0.27	0.00	-1.40
72	J061637.15+224253.3	16.76±0.16	15.39±0.12	14.74±0.08	13.63±0.03	13.13±0.04	11.74±0.31	8.40±0.00	6.83	-1.46
73	J061939.62+223711.9	16.69±0.17	15.52±0.14	14.72±0.09	13.84±0.03	13.52±0.04	11.29±0.29	8.18±0.26	2.69	-1.07

TABLE 3 continued.

ID	Catalog Number	$J(1.25\mu\text{m})$ (mag)	$H(1.65\mu\text{m})$ (mag)	$K_S(2.17\mu\text{m})$ (mag)	$W1(3.4\mu\text{m})$ (mag)	$W2(4.6\mu\text{m})$ (mag)	$W3(12\mu\text{m})$ (mag)	$W4(22\mu\text{m})$ (mag)	A_v (mag)	α
74	J061711.32+224649.4	15.80 \pm 0.07	14.71 \pm 0.06	14.21 \pm 0.05	13.50 \pm 0.03	13.01 \pm 0.04	11.29 \pm 0.27	8.49 \pm 0.34	4.25	-1.38
75	J061727.60+230007.0	16.18 \pm 0.08	15.16 \pm 0.09	14.24 \pm 0.06	13.58 \pm 0.03	12.89 \pm 0.03	10.99 \pm 0.21	8.55 \pm 0.00	0.00	-1.06
76	J061810.85+230012.3	15.56 \pm 0.06	14.50 \pm 0.05	13.89 \pm 0.05	13.22 \pm 0.03	12.77 \pm 0.03	10.93 \pm 0.20	8.67 \pm 0.40	2.65	-1.31
77	J061754.17+224851.2	15.06 \pm 0.04	14.35 \pm 0.05	14.15 \pm 0.05	13.75 \pm 0.04	13.34 \pm 0.07	10.87 \pm 0.50	7.33 \pm 0.29	0.28	-1.02
78	J061720.91+225236.4	14.75 \pm 0.03	14.21 \pm 0.05	14.08 \pm 0.05	13.77 \pm 0.03	13.34 \pm 0.05	10.15 \pm 0.12	6.86 \pm 0.14	0.00	-0.62
79	J061754.52+223312.0	14.52 \pm 0.04	14.02 \pm 0.04	13.93 \pm 0.05	13.68 \pm 0.03	13.25 \pm 0.05	11.19 \pm 0.21	8.39 \pm 0.00	0.00	-1.31
80	J061639.71+222409.3	14.55 \pm 0.04	14.11 \pm 0.05	13.94 \pm 0.05	13.61 \pm 0.04	12.78 \pm 0.06	10.52	8.14 \pm 0.28	0.00	...
81	J061718.41+222210.4	14.42 \pm 0.04	13.85 \pm 0.06	13.59 \pm 0.05	12.97 \pm 0.03	12.41 \pm 0.04	12.06	8.59 \pm 0.00	0.00	...
82	J061756.26+224600.2	13.94 \pm 0.03	13.61 \pm 0.04	13.46 \pm 0.04	13.05 \pm 0.03	12.41 \pm 0.03	10.92 \pm 0.22	7.28 \pm 0.16	0.00	-1.44
83	J061752.80+224957.8	14.99 \pm 0.07	14.25 \pm 0.07	13.92 \pm 0.05	13.41 \pm 0.04	13.00 \pm 0.04	9.82 \pm 0.09	6.99 \pm 0.15	1.20	-0.58
84	J061715.37+223141.3	16.41 \pm 0.13	15.35 \pm 0.11	14.74 \pm 0.09	13.93 \pm 0.03	13.60 \pm 0.06	11.64 \pm 0.26	8.55 \pm 0.00	2.67	-1.25
85	J061624.16+223046.2	16.91 \pm 0.19	15.69 \pm 0.16	15.40 \pm 0.18	14.07 \pm 0.04	13.79 \pm 0.07	9.68 \pm 0.07	7.32 \pm 0.12	5.85	0.12
86	J061736.65+222450.8	14.53 \pm 0.03	13.94 \pm 0.04	13.73 \pm 0.04	13.40 \pm 0.03	13.00 \pm 0.06	11.59 \pm 0.51	8.79 \pm 0.00	0.00	-1.66
87	J061823.18+224151.9	14.95 \pm 0.05	14.11 \pm 0.05	13.85 \pm 0.05	13.37 \pm 0.03	12.93 \pm 0.04	11.79 \pm 0.54	7.96 \pm 0.40	1.40	-1.77
88	J061818.14+223451.4	14.12 \pm 0.04	13.74 \pm 0.05	13.53 \pm 0.05	13.08 \pm 0.06	12.28 \pm 0.05	10.43 \pm 0.32	7.68 \pm 0.51	0.00	-1.12
89	J061809.01+223712.1	14.30 \pm 0.04	13.60 \pm 0.05	13.40 \pm 0.04	13.15 \pm 0.06	12.71 \pm 0.10	10.25	7.86 \pm 0.26	0.16	...
90	J061703.34+223629.0	14.19 \pm 0.03	13.72 \pm 0.04	13.73 \pm 0.04	13.39 \pm 0.03	12.98 \pm 0.04	10.92 \pm 0.20	8.61 \pm 0.00	0.00	-1.28
91	J061719.90+225141.2	17.25 \pm 0.23	15.81 \pm 0.15	15.17 \pm 0.11	14.30 \pm 0.05	13.46 \pm 0.06	9.68 \pm 0.06	6.68 \pm 0.08	7.16	0.03
92	J061633.37+230237.0	16.64 \pm 0.13	15.14 \pm 0.09	14.60 \pm 0.07	14.00 \pm 0.03	13.30 \pm 0.04	11.31 \pm 0.25	8.40 \pm 0.00	8.43	-1.25
93	J061725.28+225210.8	14.62 \pm 0.03	13.97 \pm 0.05	13.78 \pm 0.04	13.63 \pm 0.04	13.12 \pm 0.05	10.00 \pm 0.15	6.99 \pm 0.23	0.00	-0.68
94	J061954.07+222403.2	16.83 \pm 0.17	15.57 \pm 0.15	15.03 \pm 0.13	14.18 \pm 0.03	13.64 \pm 0.04	9.94 \pm 0.07	8.02 \pm 0.22	5.45	-0.16
95	J061656.21+225005.6	16.65 \pm 0.14	15.43 \pm 0.12	14.92 \pm 0.09	13.91 \pm 0.03	13.31 \pm 0.04	11.75	8.95 \pm 0.00	5.03	...
96	J061807.51+220431.3	16.62 \pm 0.17	15.57 \pm 0.16	14.81 \pm 0.12	13.68 \pm 0.03	13.44 \pm 0.04	9.64 \pm 0.04	7.87 \pm 0.19	1.27	-0.05
97	J061918.96+222627.3	16.58 \pm 0.15	15.52 \pm 0.14	14.82 \pm 0.10	13.63 \pm 0.03	13.30 \pm 0.04	9.37 \pm 0.04	7.13 \pm 0.11	1.89	0.09
98	J061728.02+222153.6	14.86 \pm 0.05	13.87 \pm 0.05	13.38 \pm 0.03	12.75 \pm 0.04	12.21 \pm 0.04	10.29 \pm 0.46	7.63 \pm 0.19	3.64	-1.25

The additional half-shell structure with the velocity range of -5 km s^{-1} to -2 km s^{-1} is also found to surround the northeastern half of the remnant (see Section 4.2). We suggest that the -4 km s^{-1} MCs, which are located majorly on the front of the remnant, might be close to and physically related to SNR IC 443 combining the spatial morphology of the MCs and its velocity coincidence with the shocked clumps (see Table 1). The suggestion is supported by the study of the radio spectral index distribution (see Figure 11 in Castelletti et al. 2011). In their study, the coincidence between the distribution of the flat radio spectrum and that of the high-density gas traced by CO in the interior of SNR IC 443 indicates that the strong shocks are interacting with dense ambient medium (Castelletti et al. 2011). Furthermore, the good morphological correlation between the TeV emission and the distribution of the -4 km s^{-1} MCs shows the possible connection between them (see Figure 12 in Castelletti et al. 2011).

The LSR velocities of the preshock gas for shocked clumps SC 05 and D seem to slightly deviate from -4 km s^{-1} . We consider that the velocity deviation of the two shocked clumps in the southeast of the remnant is due to the turbulence in the molecular gas. The velocity deviation between the two shocked clumps and the -4 km s^{-1} MCs can be a result of the velocity gradient within the MCs. Moreover, the ^{12}CO PV diagram (Figure 17 in Lee et al. 2012) actually shows the velocity gradient along the southeast–northwest. On the other hand, the shocked clumps E, F, and G have a similar LSR velocity at about -4 km s^{-1} and positive-velocity broad wing profiles, possibly due to the shock moving nearly transverse to our line of sight. It is not contradictory that most of the -4 km s^{-1} MCs are located on the front side of SNR IC 443.

To investigate the relationship between the shocked clump G and SCs, we made the PV diagrams along the southeast–northwest (the long arrow in the right panel of Figure 3). The arrow passes through the main body of

the -4 km s^{-1} MCs, and the PV diagrams are presented in Figure 13. The prominent broad-line wing of the ^{12}CO emission is from the shocked clump G (the left panel in Figure 13). The SCs 03 and 01 are both discerned in the PV diagrams of the ^{12}CO and ^{13}CO emission. The most attractive feature in the PV diagram of the ^{13}CO emission is that a ring structure of molecular gas (the red ellipse in Figure 13) overlaps with SC 03. In the right panel of Figure 13, the molecular ring structure with radius of $3'6$ is visible in the velocity range of -5 km s^{-1} to -3 km s^{-1} . The -6.2 km s^{-1} SC 03 shows a filamentary structure ($\sim 5' \times 2'$; see Figure 12 in Lee et al. 2012) and just superposes on the edge-on molecular ring structure. It is unlikely that the filamentary SC 03 and the molecular ring structure overlap by chance at different velocities along the line of sight. The SC 03 is possibly in physical contact with the -4 km s^{-1} MCs. Details of this ring feature will be investigated in a future paper. On the other hand the LSR velocity of SC 01 ($\sim -3.3 \text{ km s}^{-1}$) is in the range of the -4 km s^{-1} MCs (Figures 9 and 11). We suggest that the SCs seem to likely have a relation with the -4 km s^{-1} MCs.

4.2. The Half-ring Structure

We have seen that the partial shell structures of ^{12}CO emission in the northeast are concentric with the bright radio border of IC 443 and appear to confine the remnant's faint radio halo in the east. As mentioned in Section 3.1.2, we can see that the northern and northeastern partial shells, together with the eastern small clumps, form a half-ring structure to surround SNR IC 443 (the left panel in Figure 7). The LSR velocity range of the half-ring structure is consistent with the -4 km s^{-1} CO component. This is also consistent with the LSR velocity of the quiescent, ambient molecular gas of the shocked clumps B, E, F, and G (Table 1). The half-ring structure distribution along the northeastern half of the remnant indicates the high density there. On the contrary, the

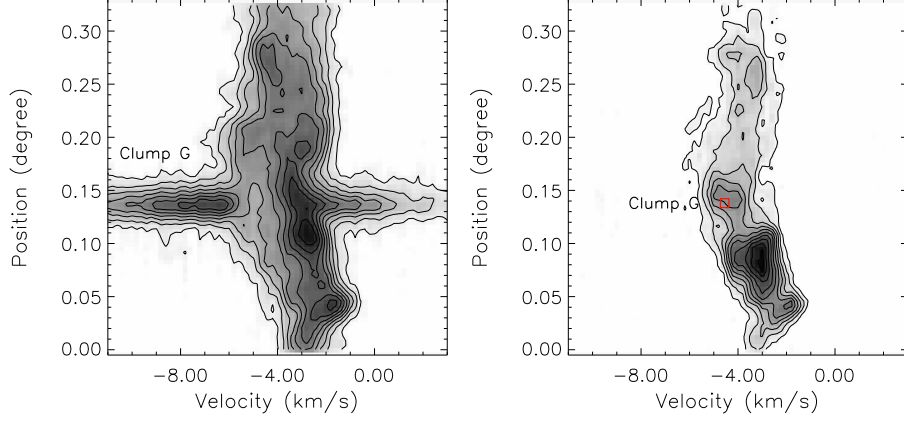


FIG. 12.— Left: position-velocity diagram of the ^{12}CO emission across the shocked clump G along the southwest-northeast (see the short arrow in Figure 3). Right: the ^{13}CO emission along the southwest-northeast. Clump G is labeled in the map. The red box indicates the position of the 1720 MHz OH maser emission.

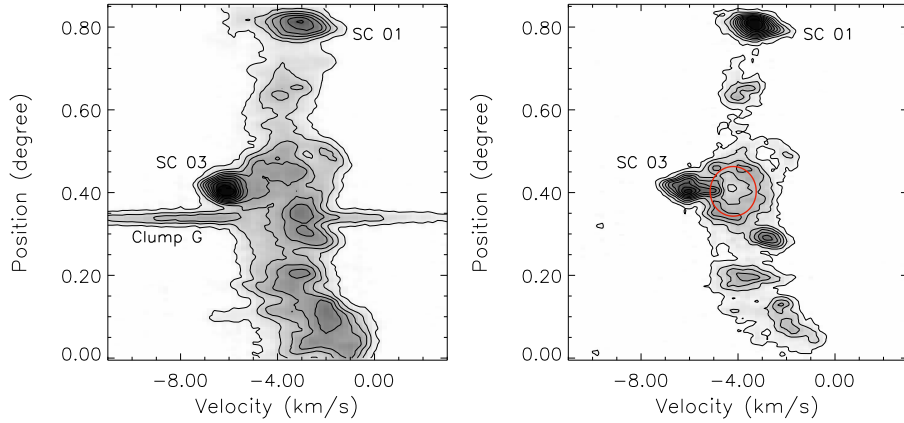


FIG. 13.— Left: position-velocity diagram of the ^{12}CO emission along the southeast-northwest (see the long arrow in Figure 3). Clumps G, SC 03, and SC 01 are labeled in the diagram. Right: the ^{13}CO emission along the southeast-northwest. The red ellipse indicates a ring structure with a radius of $3''.6$.

density is very low in the southwestern half of the remnant, in which SNR IC 443 displays the breakout structure. Moreover, the half-ring structure seems to confine the remnant's faint radio halo in the northeastern part (Figure 7).

The LSR velocity consistency between the half-ring structure and the -4 km s^{-1} MCs (Figure 3) and the positional coincidence between the ring structure and the remnant's radio halo (Figure 7) indicate that the half-ring structure with an LSR velocity of -4 km s^{-1} is associated with SNR IC 443. We also note that there are no emissions in the other bands corresponding to the half-ring structure, and the structure is unlikely shocked by the SNR. The half-ring structure is probably related to the stellar winds of the remnant's massive progenitor star (see Section 4.3).

4.3. SNR Physics of IC 443

We have shown that SNR IC 443 is located in the environment of the dense gas (Troja et al. 2008). The remnant was likely from a core-collapse explosion of a massive progenitor star, although the tail of the pulsar wind nebulae (PWNe) does not point toward the geometric center of the remnant (Olbert et al. 2001).

The scenario that SNR IC 443 is evolving inside the preexisting wind-blown bubble was suggested by several authors (Braun & Strom 1986; Troja et al. 2006, 2008; Lee et al. 2008; Yamaguchi et al. 2009). The half-ring structure (e.g., the left panel in Figure 7), which is discovered in our ^{12}CO and ^{13}CO observations, appears to confine the faint radio halo. We propose that the half-ring structure originates from the interaction between the IC 443's progenitor winds and its surrounding MCs. Assuming that the northeastern partial shell structures were formed by the gas swept by the wind of the remnant's massive progenitor, the volume ratio between the partial shell (a cylinder-like volume with a diameter of $1''.5$ and a height of $7''$ assumed) and the original rectangular pyramid (a volume with a base area of $7'' \times 1''.5$ and a height of $26''$ assumed) is about 0.14. Adopting the mean molecular density of the partial shell structures of $\sim 10^3 \text{ cm}^{-3}$ (see Section 3.1.2), the mean density in the original rectangular pyramid would be $n_m \sim 140 \text{ cm}^{-3}$ for the cloudy ISM environment. We find that the mean density of our estimation is consistent with the 170 cm^{-3} estimation of Braun & Strom (1986). The massive stellar winds will sweep a dense shell from the homogenized

region and leave a low-density bubble around the star.

Using formulae (51) and (52) in Weaver et al. (1977) and assuming $n_m \sim 140 \text{ cm}^{-3}$ and $R_2 \sim 11.3 \text{ pc}$ ($26'$ at a distance of 1.5 kpc), we compute the value of the mechanical luminosity $L_w \sim 0.6 \times 10^{34} \text{ V}_2^3 \text{ erg s}^{-1}$, which roughly corresponds to a value typical for the B0 star (Table 1 in Chen et al. 2013) for shaping a bubble with the expansion velocity of the order of magnitude of 1 km s^{-1} (Table 2). Since the expanding velocity of the half-ring structure is very low, we think that the bubble is nearly stalled in the ISM. Therefore, we use the linear relationship to assess the initial masses of the progenitors for SNRs associated with MCs (Chen et al. 2013). Considering the blowout structure of SNR IC 443, the remnant's progenitor mass of $15\text{--}19 M_\odot$ is a lower limit, which is consistent with the above calculation for a B0 star.

4.4. Star Formation in the Region of SNR IC 443

Generally, Class I objects are likely younger on average than Class II YSOs. In Figure 11 (see Section 3.2), we find that the Class I and II YSOs are much more projectively concentrated in the region of the northeastern part of SNR IC 443. Interestingly, most of Class I YSOs (blue triangles) are located along the boundary of the bright radio shell of the remnant. Because of the coincidence between the distribution of our identified YSO candidates and the remnant's morphology, it is unlikely that these YSO candidates are the foreground and background stars. Therefore we suggest that these YSOs projected on the FOV of the remnant are probably associated with SNR IC 443. Considering the age difference between the YSOs ($10^5\text{--}10^7 \text{ yr}$) and the remnant ($10^3\text{--}10^4 \text{ yr}$), we suggest that these YSOs are likely to be triggered by the stellar winds from the progenitor of IC 443 (see Section 4.3).

Xu et al. (2011) used the 2MASS All-Sky Point Source database in the near-IR $J(1.25 \mu\text{m})$, $H(1.65 \mu\text{m})$, and $K_S(2.17 \mu\text{m})$ bands to look for primary tracers of star formation activity in the vicinity of IC 443. They identified 1666 YSO candidates in a search circle around IC 443 within a $25'$ radius, whose number is greater than ours. It is probable that some YSO candidates selected by Xu et al. (2011) have flat SEDs and should be rejected (e.g., Rebull et al. 2011). We show the SED diagrams for the 98 sources in Figure 14. Actually, using 2MASS data, we identified 260 YSOs (including classical T Tauri stars and Herbig Ae/Be stars) with an S/N greater than 3. Xu et al. (2011) proposed that the distribution of YSO candidates may show a shell morphology (see Figure 5(b) in their paper). Interestingly, the similar shell structure of the distribution of our YSO candidates can be seen roughly in Figure 11. The radius of the shell structure is $\sim 20'$, which is surrounded by the radio halo of SNR IC 443.

Whitworth et al. (1994) have studied the fragmentation of the shocked dense shells swept up by an expanding stellar wind bubble. Adopting a reasonable value of $n_0 = n_m \sim 140 \text{ cm}^{-3}$, $L_w \sim 1 \times 10^{34} \text{ erg s}^{-1}$ (see Section 4.3), and the effective sound speed $a_s = 0.2 \text{ km s}^{-1}$, we can estimate the time at which the fragmentation begins, $t_{\text{fragment}} \sim 5.7 \text{ Myr}$ and the radius of the shell at that time, $R_{\text{fragment}} \sim 10.8 \text{ pc}$. This result is roughly compatible with the value of 9 pc ($20'$ at 1.5 kpc). We fit

YSO models to 75/98 sources combined 2MASS+*WISE* bands (see Columns 3–8 in Table 3) based on the work of Robitaille et al. (2007); 57/75 sources were well fitted (χ^2 less than 12). The estimated age is between 0.01 Myr and several megayears. We emphasized that the SED models are often highly ambiguous because the models show a high degree of degeneracy. Therefore, the stellar parameters are often uncertain, especially if only IR photometry is available. Spectroscopic information is needed to estimate the actual age of these YSO candidates. On the other hand, since these sources are Class I and Class II sources, the typical lifetimes for these sources are considered to be 0.5 Myr and 2–3 Myr (Evans et al. 2009), respectively. It is also compatible with the general evolutionary scheme of the progenitor's wind of SNR IC 443.

It is common that many low-mass stars will experience nearby supernovae. When a massive star dies as a supernova, the ejecta of it will expand freely through the hot, tenuous interior of an H II region. Subsequently, the gaseous ejecta from the supernova hits a protoplanetary disk to form a bow shock structure. Chevalier (2000) showed that a protoplanetary disk around a young star can survive from the nearby supernova explosion. Our solar system had very likely experienced such a process and survived from the extreme environment. Recent isotopic analysis of meteorites have revealed that the Sun and the solar system formed near a massive star and experienced a supernova explosion (Hester & Desch 2005). Briefly, the explosion of the supernova plays an essential role for the formation and evolution of the solar system (Tachibana et al. 2006).

4.5. The High-energy Emission of SNR IC 443

For SNR IC 443, the origin of the γ -ray emission is suggested to be from hadronic collisions. Abdo et al. (2010) summarized the locations and extensions of the γ -ray emission from IC 443 detected by different telescopes (e.g., EGRET: Hartman et al. 1999; MAGIC: Albert et al. 2007; VERITAS: Acciari et al. 2009; and *Fermi* LAT: Abdo et al. 2010). Based on these observations, Torres et al. (2010) used two MC models to explain the GeV–TeV connection in the vicinity of SNR IC 443. Li & Chen (2012), however, used the MC (with geometric volume) model to fit the GeV–TeV spectra. In either case, the -4 km s^{-1} MC component, for which the centroid of the molecular gas near the center of the remnant is consistent with the centroid of the GeV–TeV emission, could play an essential role for the observed γ -ray emission. Recently, Ackermann et al. (2013) identified the characteristic pion-decay feature in the gamma-ray emission. It provides direct evidence that cosmic-ray protons are accelerated in SNR IC 443. The location of the gamma-ray emission is close to the shocked clump G. For shocked clump G, the -4.4 km s^{-1} systematic velocity of the quiescent gas can be seen in Table 1, where the velocity is consistent with the result of the 1720 MHz OH observation (clump G, -4.55 km s^{-1} ; Hewitt et al. 2006). Additionally, the remarkable morphological coincidence between the TeV emission and the -4 km s^{-1} MC along the southeast–northwest (see Figure 12(c) in Castelletti et al. 2011) indicates the connection between them. Therefore, the -4 km s^{-1} MC is adjacent to SNR IC 443.

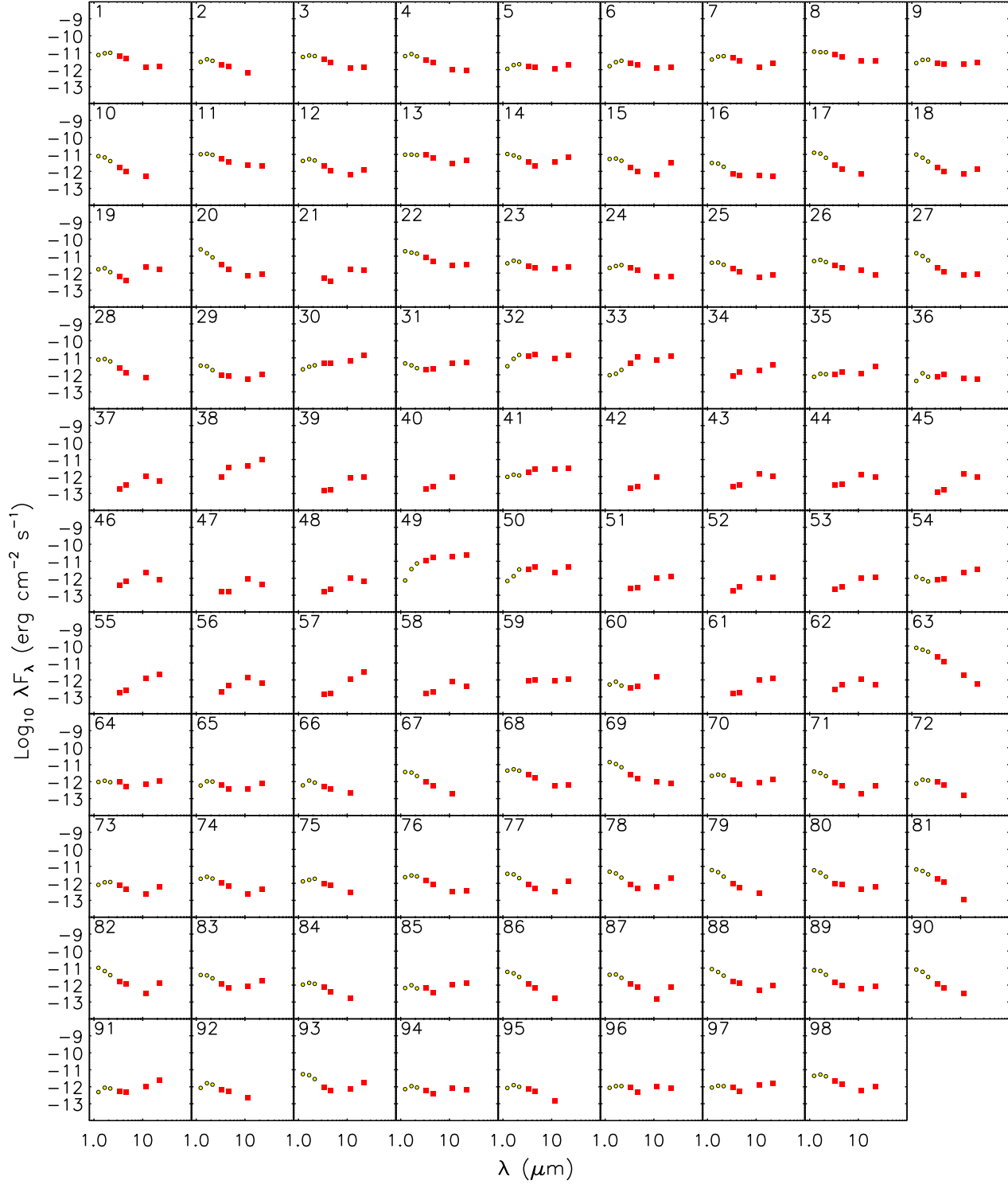


FIG. 14.— SEDs for the 98 YSO candidates. Yellow points are 2MASS data and red squares are *WISE* data. Each plot has an ID, which can be found in Table 3.

5. SUMMARY

Detailed millimeter CO studies have been performed toward SNR IC 443. By combining other multiwavelength data, we summarize the main results of our analysis as the follows.

1. The shocked clumps B–G (named from previous studies; e.g., Huang et al. 1986; Dickman et al. 1992), which appear to be connected by faint diffuse emission, are clearly identified in our new ^{12}CO maps. The spectra of these clumps are consistent with previous results.

2. The -4 km s^{-1} MC extending along the southeast–northwest is mainly located on the front of SNR IC 443. It is close to and associated with the remnant.

3. We find that a half-ring structure centered at ($06^{\text{h}}16^{\text{m}}57^{\text{s}}.1, 22^{\circ}37'06''$) with a radius of $26'$ appears to surround the northern part of SNR IC 443. We suggest that this structure in the velocity range of -5 km s^{-1} to -2 km s^{-1} is associated with IC 443. It may not be interacted with SNR IC 443 directly, but associated with the stellar winds of its massive progenitor star.

4. The progenitor of the remnant is probably a $15\text{--}19 M_{\odot}$ B0 star.

5. Sixty-two YSO candidates, mainly concentrated along the boundary of the remnant's bright radio shell, are likely to be triggered by the stellar winds from the massive progenitor of SNR IC 443.

The authors acknowledge the staff members of the

Qinghai Radio Observing Station at Delingha for their support in observation. We thank the anonymous referees for valuable advices and comments. The work also used the data from (1) the *WISE*, which is a joint project of the University of California, Los Angeles, and the Jet Propulsion Laboratory (JPL), California Institute of Technology (Caltech), funded by the National Aeronautics and Space Administration (NASA); (2) the Two Micron All Sky Survey, which is a joint project of the University of Massachusetts and the Infrared Processing and Analysis Center/California Institute of Technology, funded by NASA and the National Science Foundation; and (3) the GLIMPSE data with the *Spitzer Space Telescope*, which is operated by the Jet Propulsion Laboratory, California Institute of Technology under a contract with NASA. We also thank Dr. Lee, J. J., for providing the radio continuum data. This work is supported by NSFC grants 11103082, 11103088, 11233001, and 11233007. Y.S. acknowledges support from grant BK2011889, M.F. acknowledges support by the NSFC through grants 11203081, and Y.C. acknowledges support from the grant 20120091110048 by the Educational Ministry of China. The work is a part of the Multi-Line Galactic Plane Survey in CO and its Isotopic Transitions, also called the Milky Way Imaging Scroll Painting, which is supported by the Strategic Priority Research Program – The Emergence of Cosmological Structures of the Chinese Academy of Sciences, Grant No. XDB09000000.

REFERENCES

- Abdo, A. A., Ackermann, M., Ajello, M., et al. 2010, *ApJ*, 712, 459
- Acciari, V. A., Aliu, E., Arlen, T., et al. 2009, *ApJL*, 698, L133
- Ackermann, M., Ajello, M., Allafort, A., et al. 2013, *Sci*, 339, 807
- Albert, J., Aliu, E., Anderhub, H., et al. 2007, *ApJL*, 664, L87
- Braun, R., & Strom, R. G. 1986, *A&A*, 164, 193
- Castelletti, G., Dubner, G., Clarke, T., & Kassim, N. E. 2011, *A&A*, 534, 21
- Chen, Y., Su, Y., Slane, P. O., & Wang, Q. D. 2004, *ApJ*, 616, 885
- Chen, Y., Zhou, P., & Chu, Y. H. 2013, *ApJL*, 769, L16
- Chevalier, R. A. 2000, *ApJL*, 538, L151
- Dame, T. M., Hartmann, D., & Thaddeus, P. 2001, *ApJ*, 547, 792
- Denoyer, L. K. 1979, *ApJL*, 232, L165
- Dickman, R. L., Snell, R. L., Ziurys, L. M., & Huang, Y. L. 1992, *ApJ*, 400, 203
- Evans, N. J., II, Dunham, M. M., Jrgensen, J. K., et al. 2009, *ApJS*, 181, 321
- Fang, M., Kim, J. S., van Boekel, R., et al. 2013, *ApJS*, 207, 5
- Fesen, R. A. 1984, *ApJ*, 281, 658
- Frerking, M. A., Langer, W. D., & Wilson, R. W. 1982, *ApJ*, 262, 590
- Greene, T. P., Wilking, B. A., André, P., Young, E. T., & Lada, C. J. 1994, *ApJ*, 434, 614
- Hartman, R. C., Bertsch, D. L., Bloom, S. D., et al. 1999, *ApJS*, 123, 79
- Hester, J. J., & Desch, S. J. 2005, in *ASP Conf. Ser.* 341, Chondrites and the Protoplanetary Disk, ed. A. N. Krot, E. R. D. Scott, & B. Reipurth (San Francisco, CA: ASP), 107
- Hewitt, J. W., Yusef-Zadeh, F., Wardle, M., Roberts, D. A., & Kassim, N. E. 2006, *ApJ*, 652, 1288
- Huang, Y., Dickman, R. L., & Snell, R. L. 1986, *ApJL*, 302, L63
- Koenig, X. P., Leisawitz, D. T., Benford, D. J., et al. 2012, *ApJ*, 744, 130
- Lee, J. J., Koo, B. C., Snell, R. L., et al. 2012, *ApJ*, 749, 34
- Lee, J. J., Koo, B. C., Yun, M. S., et al. 2008, *AJ*, 135, 796
- Li, H., & Chen, Y. 2012, *MNRAS*, 421, 935
- Lockett, P., Gauthier, E., & Elitzur, M. 1999, *ApJ*, 511, 235
- Mufson, S. L., McCollough, M. L., Dickel, J. R., et al. 1986, *AJ*, 92, 1349
- Olbert, C. M., Clearfield, C. R., Williams, N. E., Keohane, J. W., & Frail, D. A. 2001, *ApJL*, 544, L205
- Rebull, L. M., Koenig, X. P., Padgett, D. L., et al. 2011, *ApJS*, 196, 4
- Reynolds, S. P., & Moffett, D. A. 1993, *AJ*, 105, 2226
- Robitaille, T. P., Whitney, B. A., Indebetouw, R., & Wood, K. 2007, *ApJS*, 169, 328
- Seta, M., Hasegawa, T., Dame, T. M., et al. 1998, *ApJ*, 505, 286
- Shan, W. L., Yang, J., Shi, S. C., et al. 2012, *IEEE*, 2, 6
- Shinn, J. H., Koo, B. C., Seon, K. I., & Lee, H. G. 2011, *ApJ*, 732, 124
- Skrutskie, M. F., Cutri, R. M., Stiening, R., et al. 2006, *AJ*, 131, 1163
- Tachibana, S., Huss, G. R., Kita, N. T., Shimoda, G., & Morishita, Y. 2006, *ApJ*, 639, 87
- Torres, D. F., Marrero, A. Y. R., & de Cea Del Pozo, E. 2010, *MNRAS*, 408, 1257
- Troja, E., Bocchino, F., Miceli, M., & Reale, F. 2008, *A&A*, 485, 777
- Troja, E., Bocchino, F., & Reale, F. 2006, *ApJ*, 649, 258
- van Dishoeck, E. F., Jansen, D. J., & Phillips, T. G. 1993, *A&A*, 279, 541
- Weaver, R., McCray, R., Castor, J., Shapiro, P., & Moore, R. 1977, *ApJ*, 218, 377
- Welsh, B. Y., & Sallmen, S. 2003, *A&A*, 408, 545
- Whitworth, A. P., Bhattal, A. S., Chapman, S. J., Disney, M. J., & Turner, J. A. 1994, *MNRAS*, 268, 291
- Wright, E., Eisenhardt, P. R. M., Mainzer, A. K., et al. 2010, *AJ*, 140, 1868
- Xu, J. L., Wang, J. J., & Miller, M. 2011, *ApJ*, 727, 81
- Yamaguchi, H., Ozawa, M., Koyama, K., et al. 2009, *ApJL*, 705, L6
- Zuo, Y. X., Li, Y., Sun, J. X., et al. 2011, *AcASn*, 52, 152